RSC Advances

PAPER

View Article Online
View Journal | View Issue

Cite this: *RSC Adv.*, 2026, **16**, 20448

A copper-mediated Fenton-like dual-mode optical sensor for sensitive determination of acetylcholinesterase activity in biological fluids

Glowi Alasiri,[a] Ali M. Alaseem,[b] Razan Orfali,[b] Mohamed M. El-Wekil,[c] Ramadan Ali,[d] Sally A. El Moumen Zohny,[e] Yasser M. Omar[f] and Al-Montaser Bellah H. Ali *[c]

Acetylcholinesterase (AChE) is a clinically important enzyme, and its accurate and sensitive determination in serum and erythrocytes is of considerable significance for biomedical and toxicological applications. Herein, a novel dual-mode optical sensing platform is reported for the quantitative determination of AChE activity, based on coupling enzymatic thiocholine generation with a copper-mediated Fenton-like redox system. AChE catalyzes the hydrolysis of acetylthiocholine to produce thiocholine, which strongly coordinates Cu(I) and suppresses copper redox cycling. In the absence of AChE, the Cu(I)/H_2O_2 system proceeds efficiently, generating hydroxyl radicals that oxidize *N*,*N*-dimethyl-*p*-phenylenediamine (DMPD) to a colored product, while concurrently formed Cu(II) quenches the fluorescence of nitrogen- and sulfur-doped carbon dots (N,S-CDs). In the presence of AChE, thiocholine production progressively suppresses radical generation and limits free Cu(II) availability, resulting in decreased absorbance and simultaneous fluorescence recovery. The fluorometric mode exhibited linearity over 0.02–0.6 mU mL^{-1} with a limit of detection of 0.0068 mU mL^{-1}, while the colorimetric mode showed linearity over a broader range of 0.1–10.0 mU mL^{-1} with a limit of detection of 0.028 mU mL^{-1}. Applied to spiked serum and erythrocyte samples, the fluorometric and colorimetric modes yielded mean recoveries of 96.50–100.50% and 96.37–102.30%, respectively. The proposed platform offers complementary sensitivity ranges, cross-validated readouts, and practical applicability in complex biological matrices, representing a reliable tool for AChE activity monitoring in clinical and environmental contexts.

Received 4th March 2026
Accepted 11th April 2026

DOI: 10.1039/d6ra01851c

rsc.li/rsc-advances

1. Introduction

Acetylcholinesterase (AChE) is a serine hydrolase enzyme that plays a pivotal role in cholinergic neurotransmission by catalyzing the rapid hydrolysis of the neurotransmitter acetylcholine into choline and acetic acid at synaptic clefts, thereby terminating nerve signal transmission.[1] It is one of the most catalytically efficient enzymes known, with a turnover rate of approximately 10 000 substrate molecules per second, and is found abundantly in the central and peripheral nervous systems as well as in erythrocytes.[2,3] Dysregulation or inhibition of AChE activity has profound physiological and pathological consequences.[4] Organophosphate and carbamate pesticides, for instance, act as potent AChE inhibitors by irreversibly or reversibly phosphorylating the enzyme's active site serine residue, leading to accumulation of acetylcholine, continuous nerve stimulation, and potentially fatal cholinergic crisis.[5] Similarly, AChE inhibition is the therapeutic mechanism underlying drugs used in the management of Alzheimer's disease, where cholinergic deficits are a hallmark feature. Beyond neurotoxicity and neurodegeneration, altered AChE activity has been implicated in cardiovascular disorders, inflammation, and certain cancers.[6] Consequently, the accurate and sensitive detection of AChE activity is of critical importance across diverse fields including clinical diagnostics, environmental monitoring, food safety, and pharmacological research, driving considerable interest in the development of rapid, sensitive, and selective analytical methods for its determination.

Acetylcholinesterase has been determined using a wide range of analytical methods, including the classical Ellman assay (DTNB/acetylthiocholine),[7] spectrophotometric and colorimetric enzymatic assays, fluorometric probes, electrochemical biosensors, chromatographic methods, and more recently nanomaterial-based and smartphone-assisted platforms.[8–10] Although these methods are widely used, many still suffer from

[a]*Department of Biochemistry, College of Medicine, Imam Mohammad Ibn Saud Islamic University (IMSIU), Riyadh 13317, Saudi Arabia*
[b]*Department of Pharmacology, College of Medicine, Imam Mohammad Ibn Saud Islamic University (IMSIU), Riyadh 13317, Saudi Arabia*
[c]*Department of Pharmaceutical Analytical Chemistry, Faculty of Pharmacy, Assiut University, Assiut, Egypt. E-mail: almontaser_bellah@aun.edu.eg*
[d]*Department of Pharmaceutical Chemistry, Faculty of Pharmacy, University of Tabuk, Tabuk 71491, Saudi Arabia*
[e]*Department of Pharmaceutical Chemistry, Faculty of Pharmacy, Sphinx University, Assiut 71515, Egypt*
[f]*Institute of Cancer Therapeutics, University of Bradford, BD7 1DP, UK*

important limitations. The Ellman method, while simple and popular, can be affected by matrix interference from thiols and colored/turbid samples, and it provides only a single optical signal with limited anti-interference capability. Electrochemical methods offer low detection limits, yet often require electrode modification, surface regeneration, and careful control of fouling in biological samples.[11,12] Chromatographic methods are more selective but typically involve expensive instrumentation, longer analysis time, and laborious sample preparation.[13,14] In addition, many reported methods rely on a single signal channel, which can reduce reliability in complex matrices and make false-positive or false-negative responses more likely.

The growing demand for sensitive, rapid, and multisignal analytical platforms has directed considerable attention toward nanomaterial-based sensing systems. Carbon dots (CDs) are a class of fluorescent carbon-based nanomaterials that have emerged as highly attractive sensing probes owing to their exceptional optical properties, including tunable emission, high quantum yield, and strong photostability, alongside low toxicity, facile synthesis, and good water solubility.[15–17] Their fluorescence can be selectively modulated by specific ions or reactive species, making them ideal candidates for the construction of fluorometric sensors. Dual-mode detection platforms, which integrate two independent and complementary transduction signals within a single analytical system, have gained increasing interest as they offer enhanced reliability, mutual cross-validation of results, and the ability to overcome the limitations inherent to single-signal methods.[18,19] The combination of colorimetric and fluorometric readouts in particular represents a powerful strategy, as it affords both instrument-free visual detection and highly sensitive quantitative measurement, broadening the applicability of the platform across resource-limited and laboratory settings alike.

The enzymatic activity of AChE is most commonly assessed using acetylthiocholine (ATCh) as a synthetic substrate, owing to its structural analogy to the natural substrate acetylcholine and the convenient detectability of its hydrolysis product. Upon AChE-catalyzed hydrolysis, ATCh yields thiocholine, a thiol-containing compound whose reactivity toward a variety of chemical and optical reporters forms the basis of numerous analytical methods. The free thiol group of thiocholine can reduce metal ions, react with chromogenic reagents, or interact with nanomaterial surfaces, enabling signal transduction in colorimetric, fluorometric, and electrochemical detection schemes. This substrate–product pair has thus become the cornerstone of indirect AChE activity assays, allowing sensitive and selective quantification of enzyme activity through the downstream chemistry of thiocholine rather than direct detection of the enzyme itself.[20,21]

This work proposes a dual-mode assay for AChE activity based on thiocholine-regulated copper Fenton-like chemistry. AChE catalyzes the hydrolysis of acetylthiocholine to generate thiocholine, a thiol product with strong affinity toward Cu(I). In parallel, Cu(I) is produced *in situ* by reducing Cu(II) with hydroxylamine·HCl, and subsequent addition of H_2O_2 drives a Cu(I)/Cu(II) redox cycle that generates hydroxyl radicals (˙OH) while converting Cu(I) back to Cu(II). The generated ˙OH oxidizes *N*,*N*-dimethyl-*p*-phenylenediamine to form a colored product for colorimetric readout, whereas the concurrently formed Cu(II) quenches the fluorescence of nitrogen- and sulfur-doped carbon dots (N,S-CDs) to provide a fluorometric signal. In the presence of AChE, the amount of thiocholine produced modulates the availability and redox cycling of copper (*via* Cu–S complexation), thereby regulating both ˙OH generation and Cu(II) formation and enabling AChE activity to be quantified through correlated changes in color intensity and carbon-dot fluorescence.

In this context, the proposed strategy offers a meaningful advance by combining thiocholine-mediated copper coordination with a Cu-based Fenton-like reaction in a dual-mode (colorimetric/fluorometric) format. The method translates AChE activity into two synchronized responses: inhibition of ˙OH-driven oxidation of *N*,*N*-dimethyl-*p*-phenylenediamine (color decrease) and reduced Cu(II)-induced quenching of N,S-CDs (fluorescence recovery). This dual-readout design improves analytical confidence compared with single-mode assays, since both channels respond to the same biochemical event but in complementary directions. The use of *in situ* generated copper redox chemistry also avoids complicated probe synthesis and supports straightforward reagent handling, while the thiocholine–copper interaction provides a direct mechanistic link between enzyme activity and signal generation. The platform is expected to provide a practical balance of sensitivity, simplicity, and matrix tolerance, with improved robustness for biological applications relative to many conventional AChE assays.

2. Experimental

2.1. Materials and reagents

Acetylcholinesterase, potassium chloride, acetylthiocholine chloride, and magnesium chloride were obtained from Sigma-Aldrich (St. Louis, MO, USA). Sodium nitrate, trypsin (Try), amylase (Amy), and pepsin were purchased from Merck (Darmstadt, Germany). Lysozyme, pancreatin, α-glucosidase, sodium chloride, and glucose oxidase (GOx) were supplied by TCI (Tokyo, Japan). Alkaline phosphatase (ALP), uricase (UOx), cholesterol oxidase (CHOD), and pyrophosphatase (PPase) were obtained from Sigma-Aldrich (St. Louis, MO, USA). Bovine serum albumin (BSA), D-glucose, calcium chloride, glycine (Gly), and L-alanine were purchased from Alfa Aesar (Ward Hill, MA, USA). L-Aspartic acid, L-leucine, phenylalanine (Phe), citric acid, thiourea and proline (Pro) were supplied by Acros Organics (Geel, Belgium). Tryptophan (Trp), histidine (His), methionine (Met), and cysteine were obtained from SRL (Mumbai, India). Glutathione (GSH), ascorbic acid (AA), and dopamine (DA) were purchased from Sigma-Aldrich (St. Louis, MO, USA). Ultrapure water (18.2 MΩ cm) was used to prepare all solutions.

2.2. Instrumentation

Complete instrumentation details are provided in the SI.

2.3. Preparation of N,S-CDs

For the hydrothermal preparation of N,S-CDs, citric acid and thiourea were first dissolved in ultrapure water at the molar

ratio (1 : 1) under magnetic stirring until a clear homogeneous solution was obtained. The resulting precursor solution was then transferred into a Teflon-lined stainless-steel autoclave (50 mL capacity, filled to no more than 80% of its volume), sealed, and heated in an oven at 200 °C for 8 h to allow carbonization and surface passivation. After naturally cooling to room temperature, the dark-colored product was collected and centrifuged (10 000 rpm for 15 min) to remove large particles/aggregates. The supernatant containing the N,S-CDs was then filtered through a 0.22 μm membrane filter and further purified by dialysis (1 kDa cutoff membrane) against ultrapure water for 48 h with periodic water replacement to remove unreacted precursors and small molecular by-products. Finally, the purified N,S-CDs solution was stored at 4 °C for further characterization and analytical use.

2.4. Quantum yield of the prepared N,S-CDs

Complete details of the quantum yield calculation are provided in the SI.

2.5. Fluorometric detection of AChE activity

For fluorometric assessment of AChE activity, varying volumes of AChE standard solution were added to a 10 mL volumetric flask containing 500 μL of acetylthiocholine (10 mM), 500 μL of N,S-CDs stock solution (1.0 mg mL^{-1}), followed by 300 μL of $CuSO_4$ solution (10 mM, prepared in hydroxylamine·HCl). Next, 500 μL of freshly prepared H_2O_2 solution (10 mM) was added and the mixture was gently mixed, then diluted to volume (10 mL) with phosphate buffer (10 mM, pH 7.0) and mixed thoroughly. The reaction mixture was incubated for 5 min at 37 °C, after which the fluorescence emission spectrum was recorded using a fluorescence spectrophotometer at an excitation wavelength of 310 nm and an emission wavelength of 490 nm, with the excitation slit width set to 5 nm.

2.6. Colorimetric detection of AChE activity

For colorimetric determination of AChE activity, varying volumes of AChE standard solution were added to a 10 mL volumetric flask containing 500 μL of acetylthiocholine (10 mM), 100 μL of DMPD solution (10.0 mM), followed by the addition of 300 μL of $CuSO_4$ solution (10 mM, prepared in hydroxylamine·HCl). Next, 500 μL of freshly prepared H_2O_2 solution (10 mM) was added and the mixture was gently mixed, then diluted to volume (10 mL) with phosphate buffer (10 mM, pH 7.0) and mixed thoroughly. The reaction mixture was incubated for 5 min at 37 °C, and the absorbance was then measured at 548 nm using a UV-vis spectrophotometer with a 1 cm quartz cuvette.

2.7. Sample preparation for AChE determination in serum and erythrocytes

Fresh human blood samples were collected in clean tubes under standard handling conditions. All procedures involving human participants were conducted in accordance with the ethical standards of the institutional research committee and with the Declaration of Helsinki. The study protocol was reviewed and approved by the Ethics Committee of Assiut University. Written informed consent was obtained from all participants prior to inclusion in the study. For serum analysis, blood was allowed to clot at room temperature and then centrifuged (4000 rpm for 10 min) to separate the serum. The collected serum was transferred to clean microtubes and stored at 4 °C for immediate analysis. Before measurement, serum samples were appropriately diluted with phosphate buffer (10 mM, pH 7.0) to bring the AChE activity within the working range of the proposed method. For recovery studies, known amounts of AChE standard were spiked into diluted serum samples. For erythrocyte (RBC) analysis, whole blood was collected in anticoagulant tubes (EDTA). The samples were centrifuged (4000 rpm for 10 min) to separate plasma and packed erythrocytes. After removal of plasma and buffy coat, the erythrocyte pellet was washed three times with cold isotonic saline (0.9% NaCl), with centrifugation after each wash to remove residual plasma components. The washed erythrocytes were then lysed by adding an appropriate volume of cold deionized water and gently mixing to obtain a hemolysate. The hemolysate was centrifuged, if necessary, to remove cell debris, and the supernatant was collected. Prior to analysis, the erythrocyte lysate was suitably diluted with phosphate buffer (10 mM, pH 7.0) to fit the calibration range. Spiked erythrocyte samples were prepared similarly for recovery evaluation. All biological samples were analyzed in triplicate, and the measured AChE activity was calculated from the corresponding calibration curve under the optimized assay conditions.

3. Results and discussion

3.1. Characterization of N,S-CDs

TEM imaging revealed that the synthesized N,S-CDs exhibit a near-spherical morphology with a uniform size distribution ranging from 3 to 8 nm and an average particle size of 5.8 nm, confirming the successful formation of well-dispersed, nanosized particles (Fig. 1A). The XRD pattern displayed a broad diffraction peak centered at $2\theta = 21.7°$, characteristic of amorphous carbon with limited graphitic ordering, which is consistent with the amorphous carbon structure typically reported for carbon dots synthesized *via* hydrothermal routes (Fig. 1B).[22] The FTIR spectrum of the N,S-CDs exhibited several characteristic absorption bands confirming the presence of multiple functional surface groups (Fig. 1C).[23] The broad absorption at 3337 cm^{-1} is attributed to O–H and N–H stretching vibrations, while the band at 2986 cm^{-1} corresponds to C–H stretching. The peak at 1652 cm^{-1} is assignable to C=O stretching of amide or carboxyl groups and C=C stretching, and the band at 1441 cm^{-1} reflects C–N stretching or O–H bending vibrations.[24,25] Peaks at 1071 and 880 cm^{-1} are associated with C–O stretching and C–S stretching vibrations, respectively, while the band at 775 cm^{-1} may be attributed to C–H out-of-plane bending. The presence of nitrogen- and sulfur-containing functional groups is consistent with the use of thiourea as the nitrogen and sulfur precursor during synthesis alongside citric acid.[26] XPS survey spectrum

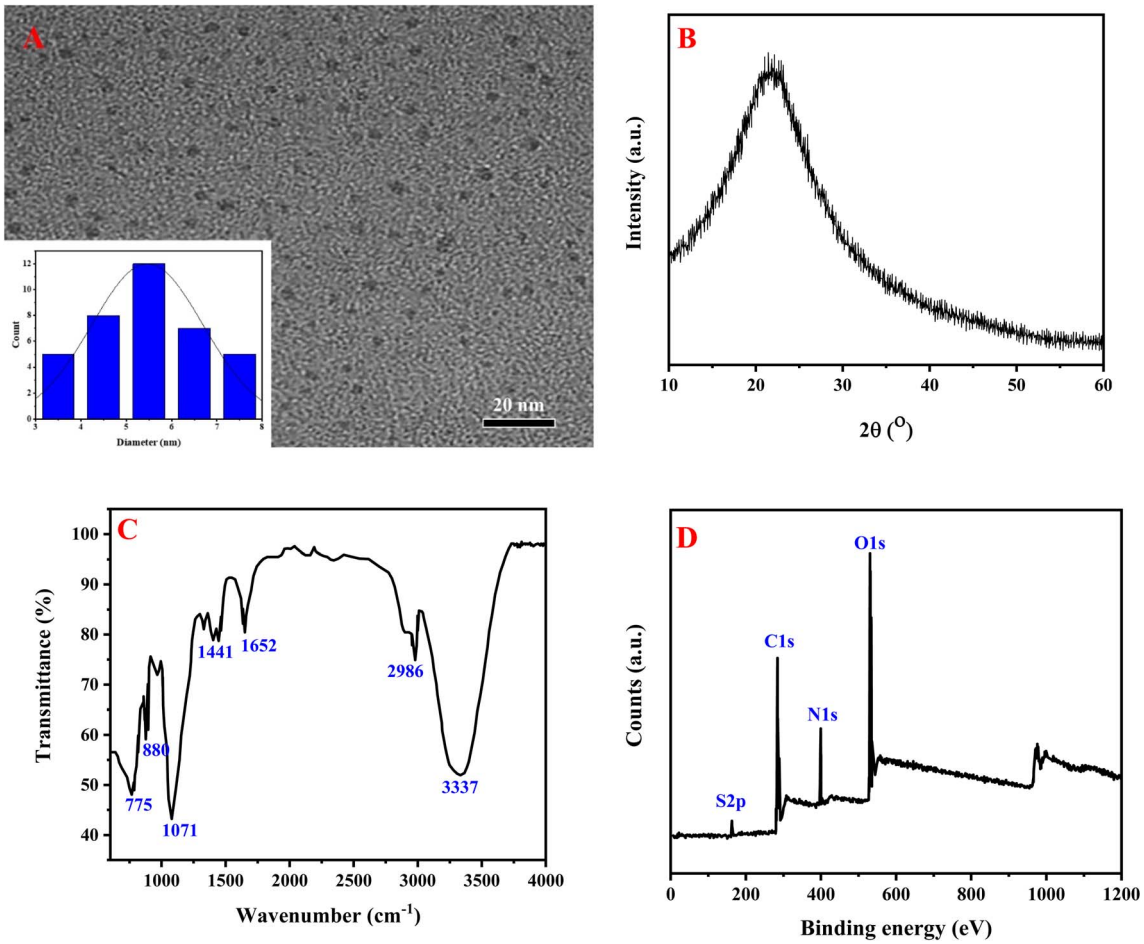

Fig. 1 (A) TEM image (inset: size distribution histogram), (B) XRD pattern, (C) FTIR spectrum, and (D) full XPS spectrum of N,S-CDs.

confirmed the elemental composition of the N,S-CDs, with characteristic binding energy peaks at 282.07, 399.72, 527.77, and 162.24 eV corresponding to C 1s, N 1s, O 1s, and S 2p, respectively, verifying successful incorporation of nitrogen and sulfur heteroatoms into the carbon framework (Fig. 1D). High-resolution deconvolution of the C 1s spectrum revealed three components at 284.76, 286.11, and 288.02 eV, assignable to C–C/C=C, C–N/C–O, and C=O/C(=O)N moieties, respectively (Fig. S1A). The N 1s spectrum was deconvoluted into two peaks at 398.97 and 400.39 eV, corresponding to pyridinic-N and pyrrolic-N or amine nitrogen, indicative of nitrogen integration within the carbon lattice and on the surface (Fig. S1B). The O 1s spectrum showed two components at 531.43 and 532.53 eV, attributed to C=O and C–O–C/C–OH functionalities (Fig. S1C), while the S 2p spectrum displayed peaks at 162.92 and 164.21 eV corresponding to S $2p_{3/2}$ and S $2p_{1/2}$ of C–S–C bonds, confirming covalent sulfur doping within the N,S-CDs structure (Fig. S1D).[27]

UV-vis absorption spectroscopy revealed three distinct absorption signals at 202.9, 231.8, and 304.5 nm, attributable to π–π* transitions of aromatic C=C bonds, n–π* transitions of C=O groups, and surface state transitions associated with nitrogen and sulfur doping, respectively (Fig. 2A).[28] Fluorescence characterization demonstrated an excitation maximum at 310 nm with a corresponding emission maximum at 490 nm. Notably, when the excitation wavelength was scanned across the range of 280–340 nm, the emission wavelength remained fixed at 490 nm while only the emission intensity varied, indicating excitation-independent emission behavior, a desirable property for quantitative analytical applications (Fig. 2B). The absolute fluorescence quantum yield of the synthesized N,S-CDs was determined to be 17.92%, reflecting satisfactory photoluminescence efficiency suitable for fluorometric sensing applications.[29]

3.2. Stability of N,S-CDs

The synthesized N,S-CDs demonstrated remarkable stability under various environmental conditions. Over the pH range of 2–12, fluorescence intensity progressively increased from acidic toward neutral and alkaline conditions, reaching maximum intensity at pH 7–12 (Fig. S2A). This behavior is attributed to the protonation state of surface functional groups (–COOH and –OH) on the carbon dots; under acidic conditions, protonation suppresses electron-donating capacity and promotes non-radiative recombination, quenching fluorescence, while deprotonation at neutral and alkaline pH stabilizes the excited state and enhances emission.[30,31] Under continuous UV

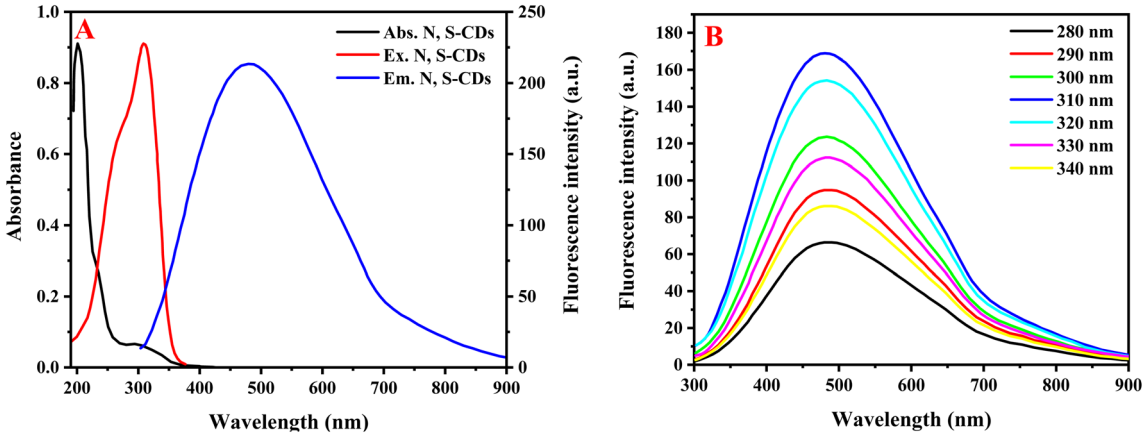

Fig. 2 (A) Absorption, excitation and emission spectra of N,S-CDs, (B) emission spectra of N,S-CDs under different excitation from 280 nm to 340 nm.

irradiation at 365 nm for 20 hours, no significant change in fluorescence intensity was observed, confirming excellent resistance to photobleaching (Fig. S2B). Furthermore, the fluorescence signal remained stable across a wide ionic strength range of 0.01–1.0 M NaCl, demonstrating tolerance to high salt concentrations (Fig. S2C). Collectively, these results confirm the robust optical stability of the N,S-CDs, supporting their suitability for reliable sensing in complex matrices.

3.3. Optimization of reaction conditions

The analytical variables affecting the proposed dual-mode AChE assay were systematically optimized to achieve maximum sensitivity and signal stability in both the fluorometric and colorimetric channels. The effect of pH was first investigated over the range 5.0–9.0, and the best response was obtained at pH 7.0 (Fig. S3A). This behavior is attributed to the need to balance two processes operating simultaneously: efficient AChE-catalyzed hydrolysis of acetylthiocholine and effective Cu-based Fenton-like redox cycling. At lower pH values, enzyme activity and thiocholine generation are reduced, while at higher pH values copper speciation and radical generation become less favorable, leading to lower signal contrast.[32] The concentration of ATCh was then scanned in the range 0.05–2.0 mM, with an optimum at 0.5 mM (Fig. S3B). Increasing ATCh concentration enhanced the response initially due to greater thiocholine production, but a plateau was observed beyond the optimum, indicating near-saturation of the enzyme and no further improvement in signal. The concentration of $CuSO_4$ was examined from 0.05 to 1.0 mM, and 0.3 mM was selected as the optimum (Fig. S3C). At low copper levels, insufficient Cu^+/Cu^{2+} redox cycling limited ROS generation and Cu^{2+}-induced quenching. The concentration of hydroxylamine·HCl, used for *in situ* reduction of Cu^{2+} to Cu^+, was scanned over 0.1–5.0 mM, and 2.0 mM gave the best analytical performance (Fig. S3D). This concentration ensured efficient Cu^+ formation and stable initiation of the Cu-Fenton-like process. Similarly, H_2O_2 concentration was scanned in the range 0.1–5.0 mM, and 0.5 mM was found to be optimal (Fig. S3E). Below this value, ROS generation was insufficient for strong DMPD oxidation and Cu^{2+} formation, while excess H_2O_2 increased the blank response and could promote non-specific oxidation, thereby lowering method sensitivity. The reaction time after mixing all reagents was studied from 1 to 15 min (Fig. S3F), and 5 min was selected because it provided rapid signal development with stable and reproducible readings; longer incubation times offered no significant improvement and tended to increase background oxidation. Finally, the concentration of DMPD was scanned between 0.05 and 1.0 mM, and 0.1 mM was chosen as the optimum (Fig. S4). At lower DMPD levels, the colorimetric response was weak.

3.4. Dual-mode detection of AChE activity

The developed dual-mode platform enables quantitative detection of AChE activity through enzyme-mediated suppression of Fenton chemistry, exploiting two complementary and independent transduction channels within a single analytical system. In the fluorometric mode, the Fenton reaction generates Cu^{2+} ions that efficiently quench the fluorescence of the carbon dots; upon introduction of AChE, the enzyme catalyzes the hydrolysis of acetylthiocholine to produce thiocholine, which in turn inhibits Cu^{2+} formation, resulting in a measurable recovery of fluorescence intensity expressed as the ratio F/F_0 (Fig. 3A). This signal exhibited a well-defined linear relationship with AChE activity over the range of 0.02–0.6 mU mL^{-1}, described by the regression equation: $F/F_0 = 1.79[\text{AChE}] + 1.08$ ($R^2 = 0.9916$) (Fig. 3B), with a limit of detection of 0.0068 mU mL^{-1}. In the colorimetric mode, Fenton-generated hydroxyl radicals ($^{\bullet}OH$) oxidize the chromogenic substrate DMPD to yield a distinctly colored product with an absorption maximum at 548 nm (Fig. 3C); as AChE activity increases, progressive depletion of $^{\bullet}OH$, leading to a concentration-dependent decrease in absorbance recorded as ΔA. This channel demonstrated linearity over a considerably broader dynamic range of 0.1–10.0 mU mL^{-1}, governed by the regression equation: $\Delta A = 0.045[\text{AChE}] + 0.068$ ($R^2 = 0.9962$) (Fig. 3D), with a limit of detection of 0.028 mU mL^{-1}. The limits of detection for both

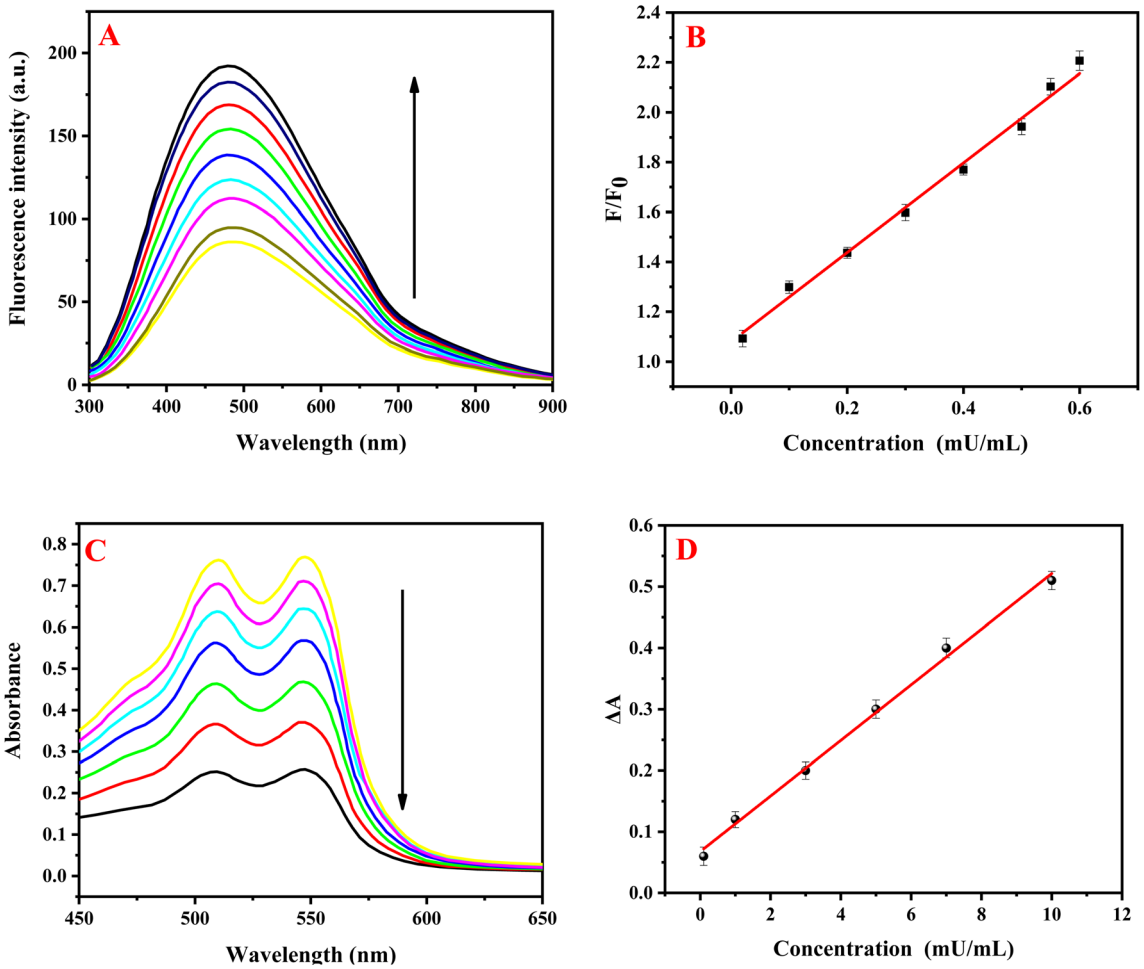

Fig. 3 (A) Emission spectra of N,S-CDs upon addition of AChE (0–0.6 mU mL^{-1}); (B) calibration curve of F/F_0 *versus* AChE concentration, showing linearity across 0.02–0.6 mU mL^{-1}. (C) Absorption spectra of oxidized DMPD upon addition of AChE (0–10.0 mU mL^{-1}); (D) calibration curve of ΔA *versus* AChE concentration, showing linearity across 0.1–10.0 mU mL^{-1}.

sensing modes were estimated using the $3\sigma/S$ method, where σ denotes the standard deviation of the blank signal obtained from ten replicate measurements and S corresponds to the slope of the calibration plot. The combined use of the colorimetric and fluorometric modes therefore provides complementary sensitivity ranges and expands the overall working range of the platform.

The analytical performance of the proposed dual-mode platform was compared with previously reported colorimetric and fluorometric methods for AChE detection (Table S1). Among colorimetric approaches, the Cu(I)/H_2O_2/DMPD system developed in this work achieved a linearity range of 0.1–10.0 mU mL^{-1} with an LOD of 0.08 mU mL^{-1}, which is superior in sensitivity to Au@PDA NPs hydrogel (LOD 0.9 mU mL^{-1})[33] and phosphorus quantum dots (LOD 0.17 mU mL^{-1}),[34] and comparable to FeMn DSAs/N-CNTs (LOD 0.066 mU mL^{-1})[35] and Fe–N–C SAzymes (LOD 0.014 mU mL^{-1}).[36] While Cu–Fe-ZIF-8/P-GCNN–H_2O_2–TMB achieved a notably lower LOD of 0.00013 mU mL^{-1},[37] this comes at the expense of considerably greater synthetic and operational complexity. In the fluorometric channel, the Cu(I)/H_2O_2/N,S-CDs system yielded an LOD of 0.0068 mU mL^{-1}, outperforming AuAgNCs (0.15 mU mL^{-1}),[38] gold nanoclusters–Cu^{2+} (0.05 mU mL^{-1}),[39] cysteine-sensing system (0.05 mU mL^{-1}),[40] and GSH–Au NCs@ZIF-8 (0.017 mU mL^{-1}),[26] and remaining competitive with ATCI–H_2O_2–OPD (0.006 mU mL^{-1}).[41] Importantly, the present platform distinguishes itself from all listed single-mode methods by offering simultaneous dual-signal readout, where the two channels provide mutually confirmatory responses, enhancing reliability and reducing false positives. Furthermore, the use of readily synthesized carbon dots and simple Fenton chemistry affords a straightforward, cost-effective, and reagent-accessible system that compares favorably in overall practicality with nanomaterial-intensive or multi-step fabrication approaches reported in the literature.

3.5. Selectivity of AChE detection

The selectivity of the proposed dual-mode AChE assay was evaluated in the presence of a wide range of potentially coexisting interferents, including enzymes and proteins (Try, Amy, pepsin, lysozyme, pancreatin, α-glucosidase, GOx, ALP, UOx, CHOD, PPase, and BSA), biomolecules and reductants (AA, DA,

GSH, D-glucose), inorganic ions (Na^+, K^+, Cl^-, NO_3^-, Ca^{2+}, and Mg^{2+}), and amino acids (Gly, L-alanine, L-aspartic acid, L-leucine, Phe, Pro, Trp, His, Met, and cysteine) (Fig. S5). Under the optimized conditions, these species produced negligible changes at their physiological levels in both the colorimetric (DMPD absorbance) and fluorometric (CD fluorescence) responses compared with the AChE-containing system, confirming the high selectivity of the method toward AChE activity. The enhanced selectivity arises primarily from the reaction-specific mechanism of the platform: only AChE catalyzes the hydrolysis of acetylthiocholine to generate thiocholine in sufficient amount, and this thiol product strongly coordinates Cu(I), thereby suppressing copper redox cycling, hydroxyl-radical generation, DMPD oxidation, and Cu(II)-induced quenching of CDs. Most tested enzymes do not recognize acetylthiocholine as a substrate, while common ions and neutral amino acids lack the required catalytic activity or strong copper-binding/reducing behavior under the assay conditions. Although some reductive species (*e.g.*, AA, DA, GSH, and cysteine) can potentially interact with copper or reactive oxygen species, their effects were minimal at the tested levels due to the controlled pH, optimized reagent concentrations, and the dual-signal readout, which improves discrimination by requiring simultaneous and consistent changes in both channels. This mechanism-based and cross-validated response profile provides strong resistance to false signals and supports reliable AChE determination in complex matrices.

Although GSH and cysteine are abundant biological thiols capable of coordinating copper, the assay maintains high selectivity for thiocholine through several complementary factors. First, thiocholine is generated enzymatically *in situ* at a locally elevated effective concentration directly at the reaction site, providing a kinetic advantage over exogenous thiols present in the bulk matrix.[42] Second, thiocholine exhibits particularly favorable thermodynamic affinity for Cu(I) owing to its compact monothiol structure and the favorable geometry of the Cu(I)–thiol complex formed, which efficiently suppresses copper redox cycling. Third, while GSH is present at millimolar concentrations in whole blood, serum GSH levels are substantially lower (2–20 μM range),[43] and appropriate sample dilution during preparation further reduces its effective concentration to levels insufficient to competitively displace thiocholine from copper coordination sites under the optimized assay conditions.[44] The dual-channel readout provides an additional safeguard, as non-specific thiol interference would need to simultaneously and consistently perturb both the colorimetric and fluorometric signals to generate a false response—a condition not met by the tested thiol species at physiologically relevant concentrations in the diluted sample matrix.

3.6. Detection mechanism of AChE activity

The proposed sensing mechanism for AChE detection is based on coupling enzymatic thiocholine generation with a copper-mediated Fenton-like redox system and dual optical signal transduction. AChE catalyzes the hydrolysis of acetylthiocholine to produce thiocholine, a thiol-containing product that strongly coordinates Cu(I) and modulates copper redox cycling. In the absence of AChE, the Cu(I)/H_2O_2 system proceeds efficiently, generating reactive oxygen species that oxidize DMPD to a colored product, while the concurrently formed Cu(II) quenches the fluorescence of carbon dots. In the presence of AChE, increasing thiocholine production suppresses copper-mediated radical generation and limits the availability of free Cu(II), resulting in decreased colorimetric response and simultaneous fluorescence recovery. Accordingly, AChE activity is quantified through synchronized, opposite-direction changes in absorbance and fluorescence intensity.

To elucidate the sensing mechanism, the quenching behavior of the N,S-CDs toward copper species was first investigated to distinguish the roles of Cu(II) and Cu(I). Independent experiments showed that the fluorescence of N,S-CDs was significantly quenched in the presence of Cu(II), whereas Cu(I) caused negligible change under identical conditions, confirming that Cu(II) is the actual quencher in the fluorometric channel (Fig. S6A). To further clarify the quenching mechanism, Stern–Volmer plots were constructed at three different temperatures (298, 318, and 338 K), yielding K_{SV} values of 2.38, 2.07, and 1.62 nM^{-1}, respectively (Fig. 4A).[45] The observed decrease in K_{SV} with increasing temperature supports a static quenching mechanism, consistent with ground-state complex formation between Cu^{2+} and the N,S-CDs surface rather than collisional quenching, as dynamic quenching would be expected to yield the opposite trend.[46] This conclusion was further validated by fluorescence lifetime measurements, which showed no significant change in the lifetime of CDs after Cu(II) addition (Fig. 4B), as static quenching typically affects fluorescence intensity without altering excited-state lifetime.[47,48] In addition, zeta potential measurements revealed a clear shift after mixing CDs with Cu(II), indicating surface interaction/complex formation between Cu(II) and functional groups on the CDs (Fig. S6B).[49]

Upon Cu(II) addition, the UV-vis spectrum exhibited a pronounced increase in absorbance across the 200–400 nm region, with the n–π* band at ~304 nm becoming notably more intense and slightly red-shifted, consistent with the formation of a Cu(II)–CD surface complex that introduces new ligand-to-metal charge transfer transitions overlapping with the existing CD absorption bands (Fig. S6C). The enhanced and broadened absorption in this region directly confirms Cu(II) coordination with the surface functional groups of the N,S-CDs, corroborating the FTIR evidence of O/N/S donor binding and supporting Cu(II)-induced fluorescence quenching as the basis of the sensing mechanism. Comparison of the FTIR spectra of N,S-CDs before and after Cu(II) addition reveals several diagnostic shifts confirming surface coordination (Fig. S6D). The broad O–H/N–H stretching band shifted from 3337 to 3275 cm^{-1}, indicating involvement of hydroxyl and amine groups in Cu(II) binding through weakening of these bonds upon coordination. The C=O/C=C band shifted from 1652 to 1588 cm^{-1}—a red-shift of ~64 cm^{-1}—consistent with electron density withdrawal from carboxyl or amide carbonyls upon metal–ligand complex formation, a hallmark of Cu–carboxylate coordination. The C–N/O–H bending band shifted from 1441 to

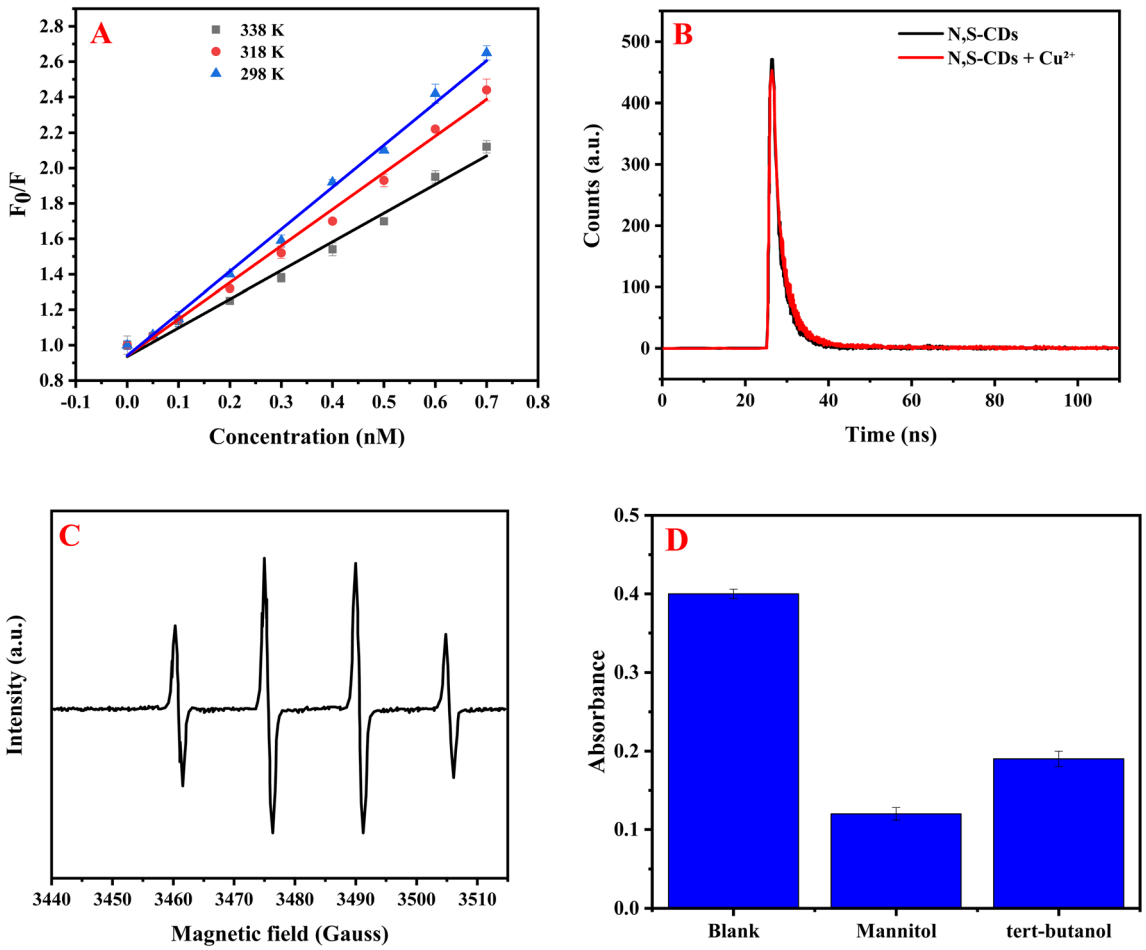

Fig. 4 (A) Stern–Volmer plots at different temperatures, (B) fluorescence lifetime of N,S-CDs before and after addition of Cu(II), (C) EPR spectrum of DMPO–OH•, and (D) absorbance of Cu(I)/H_2O_2/DMPD system in the presence of *tert*-butanol and mannitol.

1422 cm^{-1}, suggesting nitrogen participation as a donor atom in Cu–N coordination, while the C–O stretching band shifted slightly from 1071 to 1050 cm^{-1}, indicating possible oxygen involvement. Notably, the C–H stretching shifted from 2986 to 2959 cm^{-1}, and the C–S band shifted from 880 to 888 cm^{-1}, the latter confirming sulfur participation in Cu coordination consistent with the known soft-acid affinity of Cu(I/II) for sulfur donors. The band at 775 cm^{-1} shifted to 730 cm^{-1}, further reflecting perturbation of the CD surface environment. Collectively, these shifts demonstrate that Cu(II) coordinates to the N,S-CD surface through a mixed O/N/S donor coordination sphere involving carboxyl, amine, and thiol/thioether functional groups, supporting the proposed Cu–CD interaction as the mechanistic basis for Fe^{3+}-independent fluorescence quenching in the sensing platform.

The nature of the oxidizing species responsible for DMPD oxidation was then examined to verify hydroxyl radical (•OH) generation in the Cu-based Fenton-like system. Electron paramagnetic resonance (EPR) spin-trapping experiments using DMPO produced the characteristic DMPO–OH adduct signal, providing direct evidence for •OH formation (Fig. 4C).[50] To strengthen this assignment, radical scavenger experiments were performed using selective quenchers: the addition of a hydroxyl-radical scavenger (*tert*-butanol/mannitol) markedly suppressed the DMPD color response (Fig. 4D),[51] while scavengers for other reactive species produced much smaller effects. These data demonstrate that the colorimetric signal mainly arises from DMPD oxidation by •OH generated during the Cu(I)/H_2O_2 redox process, rather than by non-radical oxidants alone.[52]

To verify the role of thiocholine as the key mediator of signal modulation, independent control experiments were carried out using chemically prepared thiocholine in the absence of enzyme.[53,54] Upon adding thiocholine to the Cu(I)/H_2O_2/N,S-CDs system or Cu(I)/H_2O_2/DMPD system, both responses changed in the same direction observed in the full assay: DMPD oxidation was significantly inhibited (decreased absorbance), and N,S-CDs fluorescence quenching was attenuated (fluorescence recovery) (Fig. S6E). These findings confirm that thiocholine directly interacts with copper species—particularly Cu(I) through strong Cu–S coordination—thereby suppressing copper redox cycling, limiting •OH generation, and reducing the formation/availability of free Cu(II). Thus, thiocholine complexation with copper is the central chemical event linking enzymatic hydrolysis to both optical outputs.

Table 1 Results of recovery test of AChE in serum and erythrocyte samples ($n = 3$)

		Proposed method			HPLC method		
Sample	Method	Added (mU mL^{-1})	Found (mU mL^{-1})	Recovery (%) ± RSD%	Found (mU mL^{-1})	Recovery (%) ± RSD%	t-Test[a]
Serum	Fluorometric	0	—	—	—	—	1.21
		0.1	0.097	97.0 ± 2.32	0.098	98.0 ± 3.83	
		0.2	0.201	100.5 ± 1.91	0.195	97.5 ± 2.87	
		0.3	0.293	97.67 ± 2.89	0.29	96.67 ± 3.03	
	Colorimetric	0	—	—	—	—	0.59
		1.0	0.986	98.6 ± 2.68	1.021	102.1 ± 3.21	
		3.0	2.891	96.37 ± 3.68	2.98	99.33 ± 2.11	
		5.0	4.882	97.64 ± 2.95	4.91	98.2 ± 3.76	
Erythrocyte	Fluorometric	0	—	—	—	—	1.06
		0.1	0.099	99.0 ± 2.63	0.096	96.0 ± 1.96	
		0.2	0.193	96.5 ± 3.92	0.197	98.5 ± 2.44	
		0.3	0.298	99.33 ± 2.56	0.292	97.33 ± 2.76	
	Colorimetric	0	—	—	—	—	1.35
		1.0	1.023	102.3 ± 2.95	1.02	102.0 ± 3.96	
		3.0	2.894	96.47 ± 1.99	2.96	98.67 ± 2.85	
		5.0	5.021	100.42 ± 2.74	4.89	97.80 ± 2.16	

[a] Tabulated t-value at $p = 0.05$ is 2.23.

To further verify the interaction between thiocholine and Cu(I), the binding stoichiometry was examined by the continuous-variation method (Job's plot) under the optimized assay conditions. A series of solutions was prepared in which the total molar concentration of Cu(I) and thiocholine was kept constant, while their mole fractions were systematically varied. The signal change (ΔA) reached a maximum at a thiocholine mole fraction of approximately 0.5, indicating a 1 : 1 binding stoichiometry between thiocholine and Cu(I) (Fig. S6F). This result provides direct evidence for complex formation and supports the proposed mechanism that thiocholine coordinates with Cu(I), thereby suppressing copper redox cycling in the sensing system.

The enzymatic origin of the response was further confirmed by comparing active AChE with heat-inactivated AChE under otherwise identical conditions. The active enzyme produced the expected response (decreased DMPD absorbance), whereas the heat-inactivated enzyme caused only negligible signal changes, comparable to the blank (Fig. S7A). This clearly demonstrates that the sensing response depends on the catalytic activity of AChE rather than on nonspecific protein effects. Since heat treatment abolishes enzymatic hydrolysis of acetylthiocholine,[55] the lack of response in the inactivated control also supports that thiocholine generation is essential for modulating the copper Fenton-like system.[32,56,57]

Finally, a series of blank experiments were conducted to exclude nonspecific interactions and confirm the integrity of the dual-mode design. No significant fluorescence change was observed when N,S-CDs were treated with Cu(I) alone, indicating that Cu(I) itself does not directly produce signal without the Fenton-like reaction (Fig. S7B). Likewise, the addition of AChE alone (without acetylthiocholine substrate) caused no measurable change in either fluorescence or absorbance, confirming that the enzyme does not directly interact with CDs or DMPD to generate false signals (Fig. S7C). These blank controls, together with the mechanistic studies above, strongly support the proposed pathway in which AChE-generated thiocholine regulates a Cu-based Fenton-like process to produce synchronized fluorometric and colorimetric responses. As shown in Fig. S7D, the fluorescence spectrum of N,S-CDs remained nearly unchanged after addition of H_2O_2, with no obvious shift in emission profile or significant decrease in intensity. This result indicates that H_2O_2 does not directly affect the fluorescence of N,S-CDs under the experimental conditions.

3.7. Application of the dual-mode detection method

The accuracy and reliability of the proposed dual-mode assay were validated against an HPLC reference method by analyzing spiked serum and erythrocyte samples at three AChE activity levels in parallel.[14] The fluorometric mode yielded recoveries of 96.5–100.5% with RSD values of 1.91–3.92% ($n = 3$), while the colorimetric mode produced recoveries of 96.37–102.3% with RSD values of 1.99–3.68% ($n = 3$). The HPLC reference method returned comparable recoveries of 96.0–102.1% and RSD values of 2.16–3.96% ($n = 3$) (Table 1). All three methods demonstrated good agreement and high precision, with RSD values generally below 4%. Statistical evaluation using a paired Student's t-test at the 95% confidence level revealed no significant difference between the dual-mode assay and the HPLC method, both falling below the critical t-value, confirming the validity and practical reliability of the proposed platform for biological sample analysis.

4. Conclusions

In conclusion, a dual-mode optical sensing platform was successfully developed for the sensitive and reliable determination of AChE activity, integrating fluorometric and

colorimetric transduction channels within a single analytical system. The platform operates through a well-defined mechanistic cascade linking enzymatic thiocholine generation to copper-mediated Fenton-like chemistry, enabling synchronized and mutually confirmatory optical responses. The complementary dynamic ranges of the two detection modes collectively extend the analytical window of the platform, while their cross-validated outputs enhance result reliability and reduce the risk of false responses. The carbon dots demonstrated favorable optical properties and robust stability across varying pH, ionic strength, and prolonged UV irradiation. Validation against an HPLC reference method confirmed the accuracy and precision of both modes in complex biological matrices. Collectively, the proposed platform offers a practical, sensitive, and versatile approach to AChE activity monitoring with promising potential for application in clinical diagnostics, pharmacological screening, and environmental surveillance of AChE-inhibiting compounds.

Conflicts of interest

There are no conflicts to declare.

Data availability

Data will be available on request.

Supplementary information (SI) is available. See DOI: https://doi.org/10.1039/d6ra01851c.

Acknowledgements

This work was supported and funded by the Deanship of Scientific Research at Imam Mohammad Ibn Saud Islamic University (IMSIU) (grant number IMSIU-DDRSP2601).

References

1 L.-W. Hung, K. Y. Sanbonmatsu, R. F. Williams and J. C. H. Chen, *Protein Sci.*, 2025, **34**, e70297.
2 W. Grabowska, M. Bijak, R. Szelenberger, L. Gorniak, M. Podogrocki, P. Harmata and N. Cichon, *Int. J. Mol. Sci.*, 2025, **26**, 8726.
3 Y. Zhou, S. Wang and Y. Zhang, *J. Phys. Chem. B*, 2010, **114**, 8817–8825.
4 F. J. Luque and D. Muñoz-Torrero, *Acc. Chem. Res.*, 2024, **57**, 450–467.
5 M. B. Colović, D. Z. Krstić, T. D. Lazarević-Pašti, A. M. Bondžić and V. M. Vasić, *Curr. Neuropharmacol.*, 2013, **11**, 315–335.
6 K. Gajendra, G. K. Pratap, D. V. Poornima, M. Shantaram and G. Ranjita, *Eur. J. Med. Chem. Rep.*, 2024, **11**, 100154.
7 G. L. Ellman, K. D. Courtney, V. Andres Jr. and R. M. Feather-Stone, *Biochem. Pharmacol.*, 1961, **7**, 88–95.
8 F. Worek, P. Eyer and H. Thiermann, *Drug Test. Anal.*, 2012, **4**, 282–291.
9 D. Dingova, J. Leroy, A. Check, V. Garaj, E. Krejci and A. Hrabovska, *Anal. Biochem.*, 2014, **462**, 67–75.
10 M. Pohanka and J. Zakova, *Sensors*, 2021, **21**, 1796.
11 A. Ivanov, R. Shamagsumova, M. Larina and G. Evtugyn, *Biosensors*, 2024, **14**, 93.
12 V. Dhull, A. Gahlaut, N. Dilbaghi and V. Hooda, *Biochem. Res. Int.*, 2013, **2013**, 731501.
13 T. Tuzimski and A. Petruczynik, *Molecules*, 2021, **26**, 230.
14 S. N. Sinha, R. Ungarala, D. Kumar, R. Sangaraju and S. Kumar, *PLoS One*, 2022, **17**, e0279287.
15 S. T. Alsharif, A.-M. B. H. Ali and M. M. El-Wekil, *Spectrochim. Acta, Part A*, 2025, **339**, 126313.
16 Y. A. B. Jardan, M. M. El-Wekil, A. M. Mostafa, J. Barker and A. B. H. Ali, *Microchem. J.*, 2025, **209**, 112789.
17 F. A. M. Abdel-aal, A. M. Mahmoud, A. H. Rageh, M. R. Elmasry, Y. A. B. Jardan, M. M. El-Wekil and A.-M. B. H. Ali, *Talanta Open*, 2025, **11**, 100438.
18 A. Z. Alanazi, K. Alhazzani, A. M. Mostafa, J. Barker, H. Ibrahim, M. M. El-Wekil and A.-M. B. H. Ali, *J. Fluoresc.*, 2025, **35**, 6479–6490.
19 M. N. Goda, L. S. Alqarni, H. Ibrahim, M. M. El-Wekil and A.-M. B. H. Ali, *J. Photochem. Photobiol., A*, 2025, **468**, 116535.
20 P. C. O. de Oliveira, L. W. Tinoco, C. L. Cardoso, Q. B. Cass and M. C. de Moraes, *TrAC, Trends Anal. Chem.*, 2023, **168**, 117362.
21 N. Xia, Q. Wang and L. Liu, *Sensors*, 2015, **15**, 499–514.
22 K. J. Mintz, M. Bartoli, M. Rovere, Y. Zhou, S. D. Hettiarachchi, S. Paudyal, J. Chen, J. B. Domena, P. Y. Liyanage, R. Sampson, D. Khadka, R. R. Pandey, S. Huang, C. C. Chusuei, A. Tagliaferro and R. M. Leblanc, *Carbon*, 2021, **173**, 433–447.
23 A. Dager, T. Uchida, T. Maekawa and M. Tachibana, *Sci. Rep.*, 2019, **9**, 14004.
24 S. J. Mohammed, K. M. Omer and F. E. Hawaiz, *RSC Adv.*, 2023, **13**, 14340–14349.
25 O. Zaca-Moran, F. Díaz-Monge, A. Rodríguez-Juárez, C. L. Gómez-Muñoz, P. Zaca-Moran, O. Secundino-Sánchez and J. Díaz-Reyes, *Results Chem.*, 2024, **11**, 101788.
26 E. A. Stepanidenko, I. D. Skurlov, P. D. Khavlyuk, D. A. Onishchuk, A. V. Koroleva, E. V. Zhizhin, I. A. Arefina, D. A. Kurdyukov, D. A. Eurov, V. G. Golubev, A. V. Baranov, A. V. Fedorov, E. V. Ushakova and A. L. Rogach, *Nanomaterials*, 2022, **12**, 543.
27 R. Lamba, Y. Yukta, J. Mondal, R. Kumar, B. Pani and B. Singh, *ACS Appl. Bio Mater.*, 2024, **7**, 2086–2127.
28 P. Tiwari, N. Kaur, V. Sharma and S. M. Mobin, *J. Photochem. Photobiol., A*, 2020, **403**, 112847.
29 S. Daniel, in *Carbon Dots in Analytical Chemistry*, ed. S. K. Kailasa and C. M. Hussain, Elsevier, 2023, pp. 43–58.
30 X. Jin, X. Sun, G. Chen, L. Ding, Y. Li, Z. Liu, Z. Wang, W. Pan, C. Hu and J. Wang, *Carbon*, 2015, **81**, 388–395.
31 J. Ren, F. Weber, F. Weigert, Y. Wang, S. Choudhury, J. Xiao, I. Lauermann, U. Resch-Genger, A. Bande and T. Petit, *Nanoscale*, 2019, **11**, 2056–2064.
32 X. Orts, J. Arévalo, A. Arques, A. M. Amat and L. Santos-Juanes, *Molecules*, 2025, **30**, 2298.
33 J. Zhang, L. Mou and X. Jiang, *Anal. Chem.*, 2018, **90**, 11423–11430.
34 L. Ren, H. Li, M. Liu and J. Du, *Analyst*, 2020, **145**, 8022–8029.

35 Y.-W. Mao, J. Zhang, R. Zhang, J.-Q. Li, A.-J. Wang, X.-C. Zhou and J.-J. Feng, *Anal. Chem.*, 2023, **95**, 8640–8648.
36 Y. Wu, L. Jiao, X. Luo, W. Xu, X. Wei, H. Wang, H. Yan, W. Gu, B. Z. Xu, D. Du, Y. Lin and C. Zhu, *Small*, 2019, **15**, 1903108.
37 M. Zheng, M. Liu, F. Ma, Z. Song, H. Zhu, H. Guo and H. Sun, *Chem. Eng. J.*, 2025, **505**, 159482.
38 M. Wang, N. Li, S. Wang, J. Chen, M. Wang, L. Liu and X. Su, *Sens. Actuators, B*, 2021, **345**, 130430.
39 J. Sun and X. Yang, *Biosens. Bioelectron.*, 2015, **74**, 177–182.
40 B. Zhang and C. Wei, *ChemistrySelect*, 2017, **2**, 6844–6849.
41 X. Huang, Y. Cheng, Q. Zhou, Y. Tu and J. Yan, *Spectrochim. Acta, Part A*, 2024, **313**, 124116.
42 D. Giustarini, D. Tsikas, G. Colombo, A. Milzani, I. Dalle-Donne, P. Fanti and R. Rossi, *J. Chromatogr. B: Anal. Technol. Biomed. Life Sci.*, 2016, **1019**, 21–28.
43 N. Mahmoudi, F. Fatemi, M. Rahmandoust, F. Mirzajani and S. O. Ranaei Siadat, *Heliyon*, 2023, **9**, e19551.
44 F. Nuhu, A. Gordon, R. Sturmey, A. M. Seymour and S. Bhandari, *Molecules*, 2020, **25**, 4196.
45 K. Żamojć, W. Wiczk, B. Zaborowski, D. Jacewicz and L. Chmurzyński, *J. Fluoresc.*, 2014, **24**, 713–718.
46 Y. Song, S. Zhu, S. Xiang, X. Zhao, J. Zhang, H. Zhang, Y. Fu and B. Yang, *Nanoscale*, 2014, **6**, 4676–4682.
47 A. Kamal, S. Hong and H. Ju, *Biosensors*, 2025, **15**, 99.
48 A. López-Beltrán, C. Iriarte-Mesa, C. Murru, F. J. Chao-Mujica, A. L. Corcho-Valdés, L. Morales-Álvarez, L. F. Desdín-García, J. Deschamps and M. Antuch, *Chem.–Eur. J.*, 2023, **29**, e202300188.
49 A. M. Vervald, K. A. Laptinskiy, G. N. Chugreeva, S. A. Burikov and T. A. Dolenko, *J. Phys. Chem. C*, 2023, **127**, 21617–21628.
50 F. Peyrot, S. Lajnef and D.-L. Versace, *Catalysts*, 2022, **12**, 772.
51 F. A. Villamena, E. J. Locigno, A. Rockenbauer, C. M. Hadad and J. L. Zweier, *J. Phys. Chem. A*, 2006, **110**, 13253–13258.
52 E. W. Kellogg and I. Fridovich, *J. Biol. Chem.*, 1975, **250**, 8812–8817.
53 G. Garai-Ibabe, L. Saa and V. Pavlov, *Analyst*, 2014, **139**, 280–284.
54 S. Suzuki, Y. Nakajima, N. Kamo, A. Osakabe, A. Okamoto, G. Hayashi and H. Murakami, *Molecules*, 2023, **28**, 3655.
55 A. Komersová, K. Komers and P. Zdražilová, *Chem.-Biol. Interact.*, 2005, **157–158**, 387–388.
56 M. Fang, R. Zheng, Y. Wu, D. Yue, X. Qian, Y. Zhao and Z. Bian, *Environ. Sci.: Nano*, 2019, **6**, 105–114.
57 S. Pellegrino, P. Martínez-Marco, J. Moreno-Andrés, E. Bautista-Chamizo, A. M. Amat, C. Minero, E. Laurenti, I. Sciscenko and M. Minella, *ACS ES&T Water*, 2026, **6**, 817–829.